Proceedings of the ASME 2018 International Design Engineering Technical Conferences and Computers and Information in Engineering Conference IDETC/CIE 2018 August 26-29, 2018, Quebec City, Quebec, Canada

DETC2018-85294

A BIO-INSPIRED MINIATURE CLIMBING ROBOT WITH BILAYER DRY ADHESIVES: DESIGN, MODELING, AND EXPERIMENTATION

Audelia G. Dharmawan, Priti Xavier, David Anderson, K. Blake Perez, Hassan H. Hariri, Gim Song Soh*, Avinash Baji, Roland Bouffanais, Shaohui Foong, Hong Yee Low, Kristin L. Wood
Engineering Product Development
Singapore University of Technology and Design
Singapore 487372
Email: sohgimsong@sutd.edu.sg

ABSTRACT

This paper presents the design, modeling, and analysis of the force behavior acting on a wheel-legs (whegs) type robot which utilizes bilayer dry adhesives for wall-climbing. The motion of the robot is modeled as a slider-crank mechanism to obtain the dynamic parameters of the robot during movement. The required forces and moment to maintain equilibrium as the robot is in motion is then extensively analyzed and discussed. Following the analysis, fundamental measures to attain an operative climbing robot, such as adhesive requirement and torque specification, are then identified. The outcomes of the analysis are verified through experiments and working prototypes that are in good agreement with the design guidelines.

INTRODUCTION

The use of robots for autonomous intelligent surveillance and reconnaissance (ISR) is gaining prominence. Typical tasks include mapping, monitoring, detection, tracking, and search and rescue operations, with each requiring robots of a certain set of capabilities. Typically, these are achieved through the use of Unmanned Aerial Vehicles (UAVs) or Unmanned Ground Vehicles (UGVs), depending on the type of terrains and mission requirements. However, these robots are typically bulky to be used as solider systems, which make the use of a collaborative swarm of miniature robots to achieve these tasks attractive [1].

Compared to UAVs, UGVs have the advantage of accurately locating ground targets [2]. Various developments of miniature UGVs for autonomous ISR, each with its unique capabilities, can be found in the literature, for example spherical robot Virgo [3], reconfigurable robot Scorpio [4], jumping robot Scout [5], tracked robot MTRR [6], and climbing robot City-climber [7]. Among these, robots that are capable of scaling vertical surfaces exhibit many benefits, such as a highly-expanded workspace and the ability to reach or accomplish otherwise impossible spots or tasks. In addition, being small offers capability to navigate into tight narrow spaces, something which even UAVs find difficult due to the precision involved.

Several means can be utilized to realize climbing robots, such as through magnetic attachment [8], vacuum suction [7], gripping capability [9], and electro-adhesive technology [10]. Each approach has its own strengths and weaknesses. Magnets are strong but only work on ferrous surfaces. Suctions require bulky compressed air and completely smooth surfaces in order to establish an ideal seal. On the other hand, gripping does not work on smooth surfaces and requires looking for randomly-located handholds. Electro-adhesion requires high voltage in the order of kV. Recently, climbing robots utilizing dry adhesives have been proposed to overcome those drawbacks [11–15]. For a good review, refer to [16]. Dry adhesion is inspired by gecko's agility in climbing diverse surfaces. Using dry adhesion, robots are able to climb independent of the surface material and properties or air pressure availability. Dry adhesives are also lightweight, power

*Address all correspondence to this author.

efficient, and operationally quiet. In this paper, we utilize bilayer dry adhesives for our miniature climbing robot.

In terms of locomotion mechanism, our climbing robot has a similar structure as Mini-Whegs [17] and Waalbot [18]. It has been observed from nature that the mechanism for attachment to the surface in climbing animals is completely different from its detachment [19]. The general principle is found to be entire-surface attachment and peeling-like detachment such that strong adhesion can be instantaneously generated while minimal effort is required during contact release. For miniature robot systems, designing bulky mechanisms to fulfil this locomotion principle is undesirable. A more effective approach is to employ wheel-leg configuration with compliant adhesives to produce the required motion [20].

Despite Mini-Whegs' outstanding performance in climbing surfaces, little in-depth study can be found in the literature which theoretically models and analyzes the design requirements and capabilities of this type of robot. This paper adapts the approach in [21] to analyze our miniature climbing robot (Orion), generate its design criteria, and predict its performance. Building up from the literature, this paper expands the approach to incorporate the modeling of the movement of the robot for a more comprehensive force analysis during the motion of the robot. This paper also provides further insight on several aspects that were previously absent such as the significance of the tail effect on the overall robot's equilibrium, motor torque requirement, as well as design criteria verification.

THE CLIMBING ROBOT: ORION

Shown in Fig. 1, the architecture of our power-autonomous miniature climbing robot, Orion, consists of a robot chassis (tail) carrying the electronics and two DC motors each driving a wheel-leg (wheg) with four "flaps" equipped with bilayer dry adhesives. There is a 4:1 gear reduction between the motor and the whegs. The mass of the physical robot prototype is 71.5 g.

The bilayer synthetic gecko-inspired adhesive used here comprises of a layer of micropillar adhesive surface (polydimethylsiloxane (PDMS)) and an unstructured backing layer of

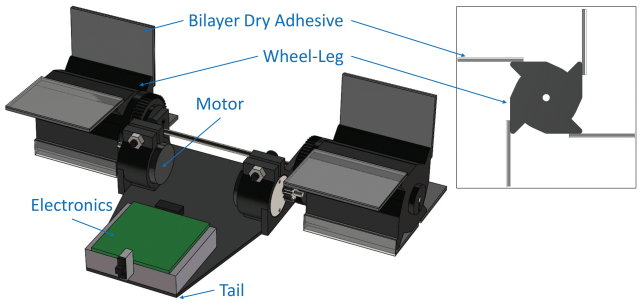

FIGURE 1. CAD MODEL OF MINIATURE CLIMBING ROBOT WITH WHEEL-LEG CONFIGURATION OF FOUR "FLAPS".

polymer (3M VHB tape) of different elastic behavior. A gradient in the viscoelastic property is thus created in the bilayer adhesive with one layer being more elastic and the other being more dissipative [22]. A series of studies has shown that a bilayer adhesive with backing layer of linearly-stiff carbon fibre in soft elastomeric adhesives imparts equal load sharing and also reduces the deformation of the soft elastomer layer [23–26]. In our case, we use a viscoelastic tape as backing layer of a lower modulus than the elastomeric adhesive due to the high energy absorption characteristic of the tape. The viscoelastic foam core of the 3M VHB tape absorbs the tensile stress, spreads the stress throughout the entire bond, and possesses high internal cohesive strength [27]. It was also observed from various reports in the literature that the addition of a foam backing layer enhances the adhesive force of PDMS [28, 29].

The elastomeric dry adhesive footpad was fabricated from elastomer PDMS, Sylgard184 (Dow Corning). PDMS is a silicone-based elastomeric polymer which is thermally-cured through a crosslinking reaction. The micro-pillars footpads were fabricated by soft lithography technique which can duplicate structures by replica molding from a SU-8 master mold (hole mold). PDMS monomer and the cross linker in the ratio of 10.5:1 were mixed and degassed in a centrifugal mixer (Thinky Mixer), poured into micro patterned SU-8 mold to the desired thickness, and cured at 80°C for 1.5 hours in a carefully-levelled oven. The PDMS is demolded from the master mold after curing. The resulting structures were pillars with 2 μm diameter, 2 μm height, and 6 μm center-to-center spacing in a hexagonal distribution (Fig. 2). The patterns were distributed as a square of area 1 cm^2,

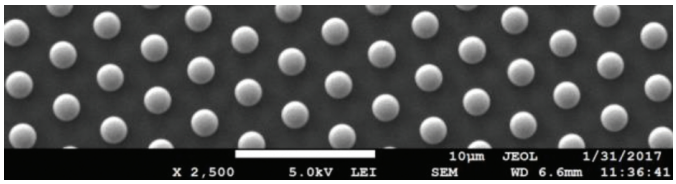

FIGURE 2. SCANNING ELECTRON MICROGRAPH OF PDMS MICROPILLARS USED IN OUR DRY ADHESIVE.

and each square patch has a distance of aproximately 1 cm^2 between each other. Hence an adhesive flap of 10 cm^2 has 5 cm^2 area with these patterns and the rest of the area is unpatterned. This adhesive was then attached to the 3M Scotch VHB tape 4607, forming a PDMS/tape composite bilayer adhesive, which is being used in the climbing robot.

ROBOT MODELING AND FORCE ANALYSIS

In this section we describe our robot locomotion model and the force analysis we performed in order to obtain the climbing robot requirements.

Robot Motion Model

To study the robot behavior during each flap contact cycle, we model the robot movement as a slider-crank mechanism to capture the dynamically changing geometric parameters for use in the force analysis. As portrayed in Fig. 3, during each flap contact cycle, the robot's movement resembles a slider-crank mechanism that rotates from $\psi = 0^\circ$ to $\psi = 90^\circ$, after which the rotational pivot switches to the next successive flap and the motion repeats. Using the analysis of the RRRP linkage [30], the positions of the pivot points **A** and **B**, and the point **C** in the coupler (representing the position of the robot's CG) relative to the frame at pivot point **O**, as shown in Fig. 4, can be expressed in terms of the input angle ζ as

$$\mathbf{A} = \begin{Bmatrix} r\cos\zeta \\ r\sin\zeta \end{Bmatrix} \tag{1}$$

$$\mathbf{B} = \begin{Bmatrix} s \\ e \end{Bmatrix} \tag{2}$$

$$\mathbf{C} = \begin{Bmatrix} r\cos\zeta + d\cos(\zeta+\phi-\alpha) \\ r\sin\zeta + d\sin(\zeta+\phi-\alpha) \end{Bmatrix} \tag{3}$$

where

$$s = r\cos\zeta - \sqrt{L^2 - e^2 + 2er\sin\zeta - (r\sin\zeta)^2} \tag{4}$$

$$\phi = \arctan2\left(\frac{e - r\sin\zeta}{s - r\cos\zeta}\right) - \zeta \tag{5}$$

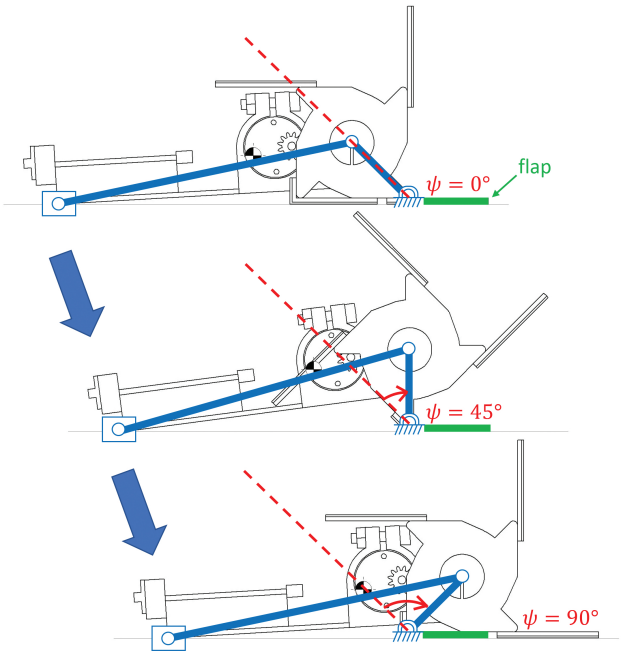

FIGURE 3. SLIDER-CRANK MECHANISM MODEL FOR THE ROBOT MOTION.

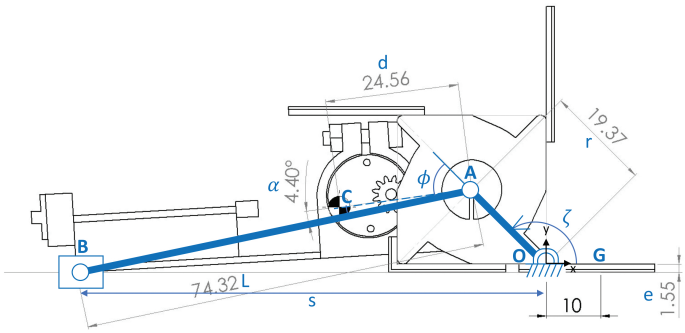

FIGURE 4. GEOMETRIC PARAMETERS OF THE ROBOT.

Note that the robot's motion of $\psi = 0^\circ$ to $\psi = 90^\circ$ in Fig. 3 is equivalent to the slider-crank input rotation of $\zeta = 135^\circ$ to $\zeta = 45^\circ$ in Fig. 4, i.e. $\zeta = 135^\circ - \psi$. Using this motion model, the changing geometric parameters of the robot can be captured continuously as it moves, and the force analysis can be performed throughout the robot motion.

Adhesive Force Requirement Analysis

Adhesives generally have high shear adhesion strength and detachment usually occurs due to insufficient normal adhesion. As seen in Fig. 3, there are generally two states of the robots: double-flap stance and single-flap stance. Similar to [21], the minimum normal adhesive force required to prevent detachment is analyzed at the single-flap stance as there is only one flap per side attached to the surface providing adhesion. However, instead of assuming that the highest adhesion required is at $\psi = 45^\circ$ (due to the robot's CG being the furthest away from the surface), we analyze the required normal adhesive force for the entire robot motion and demonstrate that the assumption does not necessarily hold. Although the peeling motion in whegs is gradual, i.e. there exists double-flap stance between $\psi = 0^\circ$ to $\psi = 90^\circ$, the instances are simplified and the analysis of the single-flap stance is performed for the whole motion of the robot, as getting a higher minimum adhesive force than required does not deteriorate the design criteria but rather adds a decent safety margin. The green adhesive in Fig. 3 is the single flap of interest that provides the adhesion to the surface during the robot motion.

Quasi-static analysis is usually adequate when the robot is moving slowly or at a constant velocity. In addition, assuming symmetric loading and an equivalent point force acting at the center of the adhesive (**G** in Fig. 4), the system of equations for equilibrium during single-flap stance (Fig. 5(a)) is given by

$$\sum F_x = 0 = F_{Rxm} - W\sin\theta \tag{6}$$

$$\sum F_y = 0 = F_{tm} + F_{Rnm} - W\cos\theta \tag{7}$$

$$\sum M_P = 0 = F_{tm}L_{tm}(\psi) - W\cos\theta(L_{xcgm}(\psi)) - W\sin\theta(L_{ycgm}(\psi)) - F_{Rnm}L_{xrm} \tag{8}$$

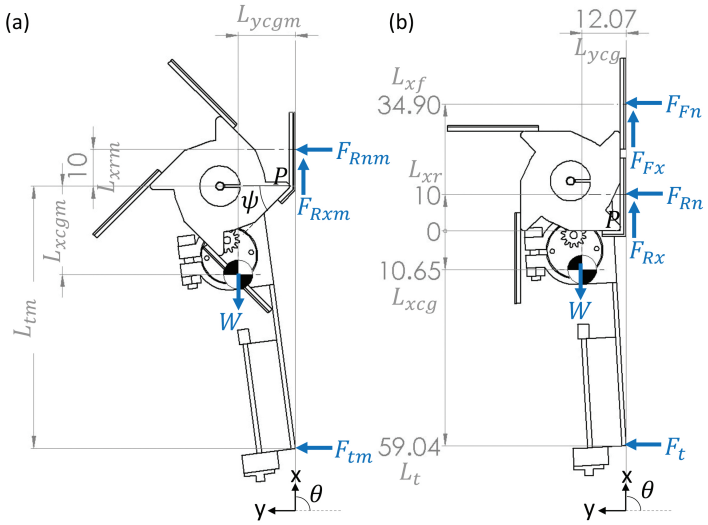

FIGURE 5. FREE BODY DIAGRAM OF THE CLIMBING ROBOT (a) DURING SINGLE-STANCE MOTION (b) DURING DOUBLE-STANCE (DIMENSIONS ARE IN MM).

where θ is the climbing slope angle, W is the robot's weight, F_{Rxm} is the shear force on the adhesive flap, F_{Rnm} and F_{tm} are the normal forces on the adhesive and the tail respectively, L_{tm}, L_{xcgm}, and L_{xrm} are the distances between the pivot point P and the tail, CG, and the center of the adhesive respectively, L_{ycgm} is distance between the slope surface and the CG, and ψ is the wheel rotation angle. Solving for F_{Rnm} gives

$$F_{Rnm} = \frac{W\left[\cos\theta\left(L_{tm}(\psi) - L_{xcgm}(\psi)\right) - \sin\theta\left(L_{ycgm}(\psi)\right)\right]}{L_{tm}(\psi) + L_{xrm}} \quad (9)$$

which gives the normal force acting at the center of the adhesive during the single-stance motion at each instance ψ for different slope angle θ, and where

$$L_{tm}(\psi) = -B_x(\psi) \quad (10)$$

$$L_{xcgm}(\psi) = -C_x(\psi) \quad (11)$$

$$L_{ycgm}(\psi) = C_y(\psi) - B_y(\psi) \quad (12)$$

Figure 6 (top) shows the plot of the normal force acting on the adhesive (F_{Rnm}) for the single-flap stance at varying climbing slopes θ. The blue dotted line denotes the values of F_{Rnm} at $\psi = 45°$, which is the wheel rotation angle at which the robot's CG is the furthest away from the slope. The blue solid line plots the minimum value of F_{Rnm} along the robot motion, and the orange dash-dot line shows the wheel rotation angle ψ at which the minimum F_{Rnm} occurs. For example, at 100° slope, the minimum F_{Rnm} is -0.22 N and the wheel rotation angle ψ at which this occurs is 69°. Hence, one can see that the minimum force

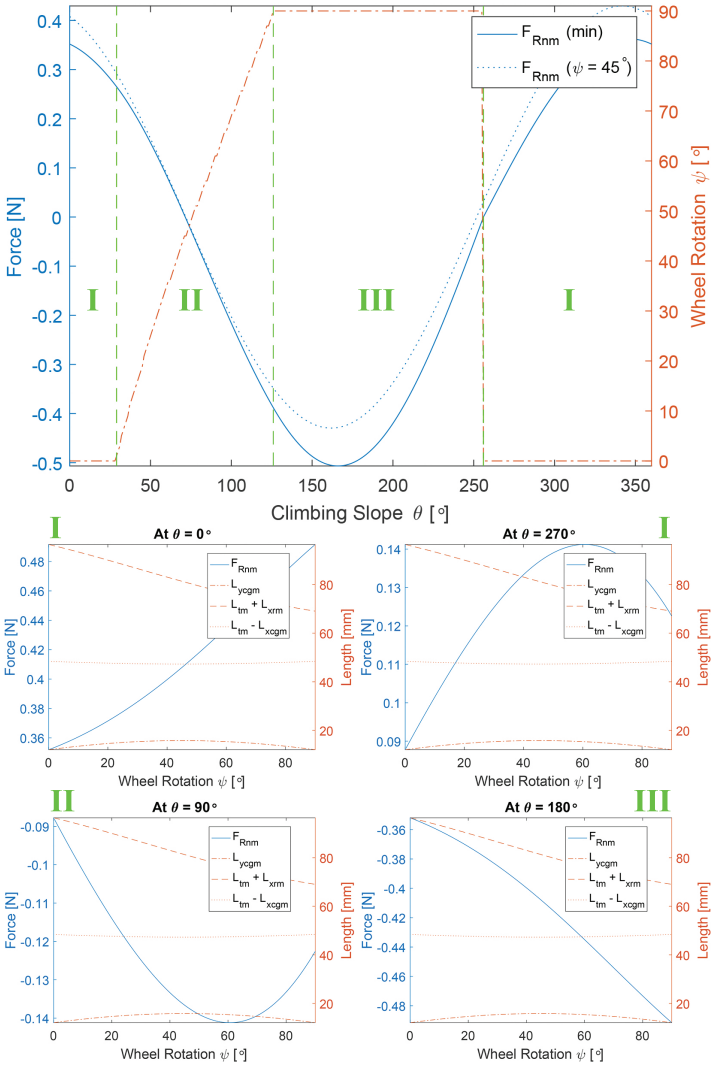

FIGURE 6. PLOT OF THE NORMAL FORCE AT THE CENTER OF THE ADHESIVE DURING SINGLE-FLAP STANCE VERSUS SLOPE ANGLE (TOP), AND ALONG THE ROBOT MOTION AT SEVERAL SPECIFIC SLOPE ANGLES (BOTTOM SUBPLOTS).

does not always occur at $\psi = 45°$; in fact it smoothly progresses from $\psi = 0°$ to $\psi = 90°$ for an interval of the slope angles before settling at either $\psi = 0°$ or $\psi = 90°$. This is because, as can be inferred from Eq. (9), the minimum F_{Rnm} is not only affected by the distance of the robot's CG from the surface but also by the relative distance of the robot's tail from other parts of the robot.

Zooming in into details, the robot position where minimum F_{Rnm} occurs for the varying climbing slopes θ (Fig. 6 top) can generally be divided into three regions (Fig. 6 bottom subplots): (I) $F_{Rnm}(\psi)$ increases along the robot motion or is concave and minimum F_{Rnm} occurs at $\psi = 0°$, (II) $F_{Rnm}(\psi)$ is convex and minimum F_{Rnm} progressively occurs at $\psi = 0°$ to $\psi = 90°$, and (III) $F_{Rnm}(\psi)$ decreases along the robot motion or is concave and

minimum F_{Rnm} occurs at $\psi = 90°$. This is analogous to scanning a general graph of "$a\cos(x) - b\sin(x)$" with varying amplitudes, which is foreseen from the structure of Eq. (9).

Tail Force Analysis

For a more comprehensive analysis of the factors affecting the normal force on the adhesive, we now further analyze the force acting on the robot's tail as well. Fig. 7 shows the plot of the minimum normal force on the adhesive for varying slope angles, and the corresponding normal force acting on the robot's tail (F_{tm}) obtained through Eq. (7). Fundamentally, adhesion is required when these forces are negative, as this means that instead of experiencing a positive reaction (pushing) force from the surface, the robot experiences an attractive (pulling) force, which should be provided by the adhesion.

As seen in Fig. 7, F_{tm} falls below zero for a range of slope angles. This means that adhesion at the robot's tail is sometimes needed to maintain equilibrium. However, there is no adhesion at the tail of our robot, and when F_{tm} is negative, the tail in fact loses contact with the surface. In light of this, we now introduce another two distinct states of the robot: (1) the tail is in contact with the surface, and (2) the tail loses contact with the surface. When the second state occurs, we need to set F_{tm} to zero instead. Then, from Eq. (7), F_{Rnm} bears all the y-component of the robot's weight, i.e. $F_{Rnm} = W\cos\theta$. The moment component initially provided by the tail ($F_{tm}L_{tm}$ in Eq. (8)) now needs to be provided by the moment component of the adhesion (termed as M_{Rm} hereafter), which was assumed to be zero or non-existent in the previous analysis. In summary,

State 1 Robot's tail is in contact with the surface ($F_{tm} > 0$)

$$F_{Rnm} = \frac{W\left[\cos\theta\left(L_{tm}(\psi) - L_{xcgm}(\psi)\right) - \sin\theta\left(L_{ycgm}(\psi)\right)\right]}{L_{tm}(\psi) + L_{xrm}}$$
$$F_{tm} = W\cos\theta - F_{Rnm}$$
$$M_{Rm} = 0 \qquad (13)$$

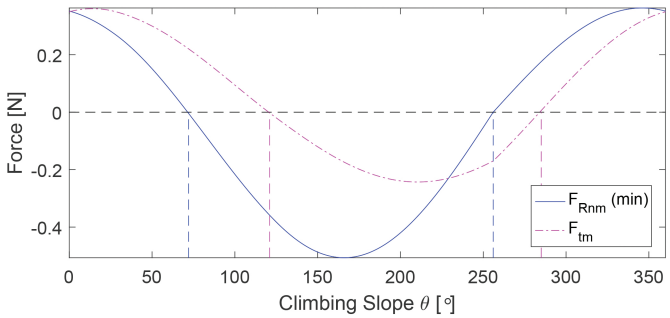

FIGURE 7. PLOT OF THE MINIMUM NORMAL FORCE AT THE CENTER OF THE ADHESIVE DURING SINGLE-FLAP STANCE, AND THE CORRESPONDING NORMAL FORCE ACTING ON THE ROBOT'S TAIL FOR VARYING SLOPE ANGLES.

State 2 Robot's tail loses contact with the surface ($F_{tm} \leq 0$)

$$F_{Rnm} = W\cos\theta$$
$$F_{tm} = 0$$
$$M_{Rm} = -W\cos\theta\left(L_{xcgm}(\psi)\right) - W\sin\theta\left(L_{ycgm}(\psi)\right) - F_{Rnm}L_{xrm} \qquad (14)$$

Figure 8 shows the plots of the minimum normal forces on the adhesive obtained using the different analysis approaches, with F_{Rnm} (rev) and F_{tm} (rev) being the results of the revised analysis in this section. As seen from the figure, fixing the force analysis at $\psi = 45°$ and without analyzing the force behavior at the robot's tail leads to an underestimation of the minimum adhesive force required. It is also more sensible to set $F_{tm} = 0$ when $F_{tm} \leq 0$, as following the previous analysis (F_{Rnm} (min)), one would have expected the robot (without adhesive at the tail) to be able to climb a 260° slope without the need of an adhesive on the wheels, which is not the case. The revised analysis (F_{Rnm} (rev) in Fig. 8) gives a more reasonable prediction as the robot is expected to stop needing an adhesive for slopes above 270° (climbing vertical down).

Based on the minimum normal force acting on the adhesive (F_{Rnm} (rev) in Fig. 8), we can then decide on the required value of the *critical peeling force*, F_{cr}, of the adhesive material according to the slope angle that the robot needs to be able to climb, with $F_{cr} = -F_{Rnm}$. For example in our case, we want to design a robot that is able to climb up to 120° slope, so the critical peeling force of the adhesive material used should be at least 0.36 N, as shown in Fig. 8 (red dashed line).

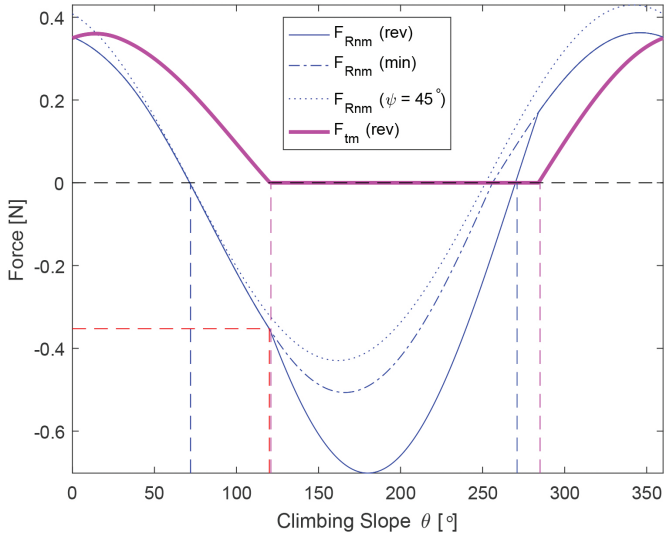

FIGURE 8. PLOT OF THE MINIMUM NORMAL FORCE AT THE CENTER OF THE ADHESIVE DURING SINGLE-FLAP STANCE BASED ON THE DIFFERENT ANALYSIS APPROACHES, AND THE FORCE ACTING ON THE ROBOT'S TAIL BASED ON THE TAIL FORCE ANALYSIS, FOR VARYING SLOPE ANGLES.

Preload-to-Peeling Force Ratio Analysis

Another important measure in the modeling of climbing robots with dry adhesives is the preload-force-to-critical-peeling-force ratio, as adhesive material is usually characterized by how much adhesive force can be generated by a given preload force. Analyzing the double-flap stance (Fig. 5(b)), it can be inferred that at this stage the rear flap is peeling the adhesive while the front flap is being preloaded simultaneously. Assuming that peel-off is just about to occur, then $F_{Rn} = -F_{cr}$, and F_{Fn} gives the preload force applied on the front flap. The system of equations for equilibrium during double-flap stance (Fig. 5(b)) is given by

$$\sum F_x = 0 = F_{Rx} + F_{Fx} - W\sin\theta \tag{15}$$

$$\sum F_y = 0 = F_t + F_{Rn} + F_{Fn} - W\cos\theta \tag{16}$$

$$\sum M_P = 0 = F_t L_t - W\cos\theta(L_{xcg}) - W\sin\theta(L_{ycg}) - F_{Rn}L_{xr} - F_{Fn}L_{xf} \tag{17}$$

from which we can solve for F_{Fn} with the geometric dimensions of the robot as given in Fig. 5(b). Similarly, there are two states of the robot,

State 1 Robot's tail is in contact with the surface ($F_t > 0$)

$$F_{Fn} = \frac{W\left[\cos\theta(L_t - L_{xcg}) - \sin\theta(L_{ycg})\right] - F_{Rn}(L_t + L_{xr})}{L_t + L_{xf}}$$
$$F_t = W\cos\theta - F_{Rn} - F_{Fn}$$
$$M_R + M_F = 0 \tag{18}$$

State 2 Robot's tail loses contact with the surface ($F_t \leq 0$)

$$F_{Fn} = W\cos\theta - F_{Rn}$$
$$F_t = 0$$
$$M_R + M_F = -W\cos\theta(L_{xcg}) - W\sin\theta(L_{ycg}) - F_{Rn}L_{xr} - F_{Fn}L_{xf} \tag{19}$$

where M_R and M_F are the moment components of the rear and front adhesive respectively. The preload-to-critical-peel-off ratio (R_{pp}) can then be obtained as F_{Fn}/F_{cr} and is plotted in Fig. 9. Negative values of the ratio indicate the range of climbing slopes that the robot is unable to climb due to the choice of the critical peeling force F_{cr} value of the adhesive material. This ratio will be useful in devising further requirements for the adhesive material, which will be discussed in the next section.

CLIMBING ROBOT REQUIREMENTS

In this section, we discuss two important design criteria that can be obtained following the force analysis, namely the minimum adhesive size to generate the required adhesion force based on the material characteristics, and the minimum motor torque required to provide the peeling and preload forces, overcome the robot's weight component along the slope, and keep the overall equilibrium of the climbing robot. These two criteria must be met in order to attain an operative climbing robot, which can serve as constraints for robot optimization.

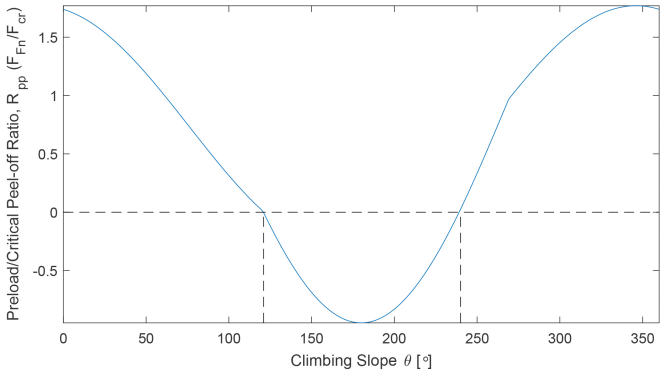

FIGURE 9. PLOT OF THE PRELOAD-TO-CRITICAL-PEELING FORCE RATIO FOR VARYING SLOPE ANGLES.

Adhesive Size Requirement

Adhesive material is characterized by how much adhesive force is generated given a preload force. Typically, adhesion is greater than preload for low preload pressures and saturates to a maximum adhesion value at high preload pressures, which can be approximated by a power law function [21],

$$P_A = a P_P^{1/n} \tag{20}$$

where P_A is the adhesion pressure, P_P is the preload pressure, a is a scaling coefficient, and $n > 1$. The characteristics of the dry adhesive that we use is comparable to common PDMS and we obtain its adhesion performance from literature [31], which can be approximated by $P_A = 0.06 P_P^{\frac{1}{13.85}}$. In order to identify the suitable size of the adhesive material, the adhesion vs preload curve is overlayed with lines of gradient values corresponding to the inverse of the preload-to-peeling ratio R_{pp} at various climbing slope angle θ (Fig. 9),

$$P_A = \frac{1}{R_{pp}(\theta)} P_P. \tag{21}$$

This is shown in Fig. 10 for some slope angles. The intersection of the performance curve and this inverse-ratio line then gives the specific preload pressure that multiplies into the required amount of adhesion pressure according to the preload-to-peeling ratio, which can be obtained as

$$P_P{}^* = (a R_{pp})^{\frac{n}{n-1}} \tag{22}$$

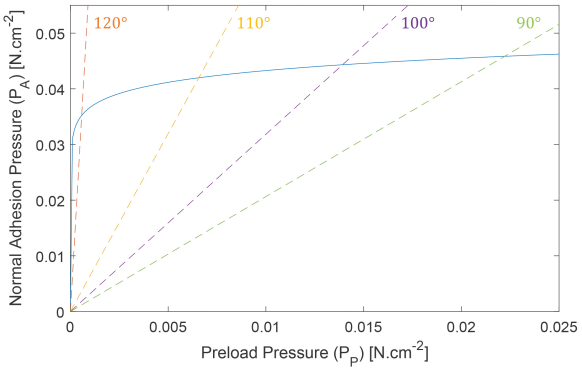

FIGURE 10. ADHESIVE PERFORMANCE CURVE OVERLAYED WITH LINES OF GRADIENT VALUES OF THE INVERSE OF THE PRELOAD-TO-PEELING RATIO FOR SEVERAL SLOPE ANGLES.

The minimum required adhesive area (A_a) is then obtained by

$$A_a = \frac{F_{Fn}}{P_P^*} \tag{23}$$

Based on this analysis, our robot is required to have a minimum adhesive area of 5 cm^2 per flap to be able to climb up to 120° slope angle.

Motor Torque Requirement

To obtain the minimum motor torque required, the free body diagram (FBD) of the whole robot is decoupled into the wheel and chassis components as shown in Fig. 11. The values of the normal forces acting on the adhesive and the tail will follow the revised analysis based on the robot motion and tail consideration (F_{Rnm} (rev)). From the chassis FBD (Fig. 11(c)) we have

$$\sum F_x = 0 = -R_x - W\sin\theta \tag{24}$$

From the single-flap stance wheel FBD (Fig. 11(a)) we have

$$\sum F_x = 0 = F_{Rxm} + R_x \tag{25}$$

$$\sum M_S = 0 = T_{s,1} - F_{Rnm}(L_{xrsm}(\psi)) - F_{Rxm}(L_{yrsm}(\psi)) - M_{Rm} \tag{26}$$

where

$$L_{xrsm}(\psi) = G_x - A_x(\psi) \tag{27}$$

$$L_{yrsm}(\psi) = A_y(\psi) - B_y(\psi) \tag{28}$$

Then we can get the torque acting on the shaft at single-flap stance along the robot motion as

$$T_{s,1} = F_{Rnm}(L_{xrsm}(\psi)) + W\sin\theta(L_{yrsm}(\psi)) + M_{Rm} \tag{29}$$

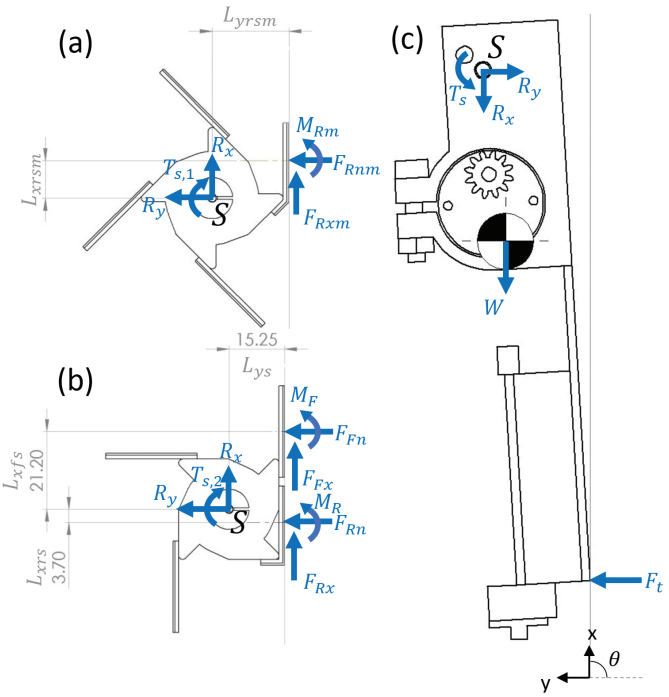

FIGURE 11. FREE BODY DIAGRAM OF THE INDIVIDUAL COMPONENTS OF THE ROBOT: (A) WHEEL AT SINGLE-FLAP STANCE, (B) WHEEL AT DOUBLE-FLAP STANCE, AND (C) CHASSIS.

Similarly from the double-flap stance wheel FBD (Fig. 11(b)) we have

$$\sum F_x = 0 = F_{Rx} + F_{Fx} + R_x \tag{30}$$

$$\sum M_S = 0 = T_{s,2} + F_{Rn}(L_{xrs}) - F_{Fn}(L_{xfs}) - (F_{Rx} + F_{Fx})L_{ys} - M_R - M_F \tag{31}$$

The torque acting on the shaft during double-flap stance is then obtained as

$$T_{s,2} = F_{Fn}(L_{xfs}) - F_{Rn}(L_{xrs}) - W\sin\theta(L_{ys}) + M_R + M_F \tag{32}$$

Then, the minimum motor torque requirement is obtained as

$$T_m = \frac{max(max(T_{s,1}), T_{s,2})}{R_g} \tag{33}$$

where R_g is gear reduction value (if any).

Fig. 12 shows the minimum motor torque required by our robot to climb the varying slope angles with adhesive material of critical peeling force $F_{cr} = 0.36$ N. Note that since our robot is driven by two separate motors, the required torque is shared by the two motors.

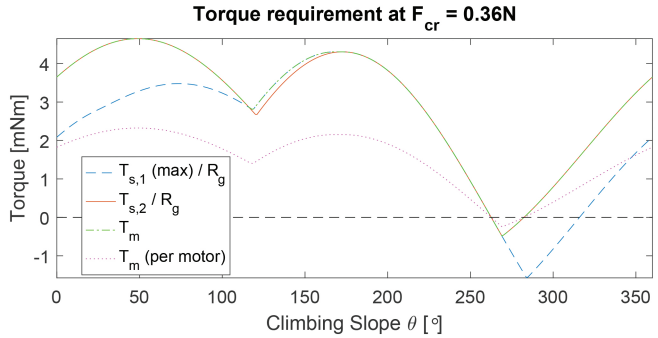

FIGURE 12. PLOTS OF THE TORQUE REQUIREMENTS FOR VARYING SLOPE ANGLES FOR $F_{cr} = 0.36$ N.

EXPERIMENTS

In this section, we perform experiments on the physical climbing robot protoype to verify the validity of the revised force analysis and the design criteria generated.

Force Evaluation

To verify the normal force acting on the adhesive along the robot's motion, one of the robot's legs was adhered to a digital scale to measure the normal force at three different single-flap stance configurations as shown in Fig. 3. These measurements were taken at a climbing slope interval of 45°, and the results are shown in Fig. 13 (top). It was quite hard to get reliable measurements at robot's configuration $\psi = 0°$ and $\psi = 45°$ for climbing slope angles 180°, 225°, and 270°, as the robot tended to slowly rotate away from the surface under its own weight (pitch-back) due to the compliancy of the adhesive. At $\psi = 90°$, this pitch-back moment was couteracted by the higher bending moment of the adhesive at the higher bending angle, and thus measurement could be taken. In light of this, the force measurement at the tail was only performed at configuration $\psi = 90°$ so that it was not affected by the pitch-back motion. For the tail force measurement, the robot's tail was also placed on a digital scale (without adhesive), and the force measurement results are shown in Fig. 13 (bottom). Based on the experimental results, it is verified that the force behavior during the robot's motion can be attained fairly accurately using the robot motion model. The experimental results also validate that the normal force at the tail became zero when it loses contact with the sensor (i.e. the surface) instead of experiencing a negative force, and the corresponding force on the adhesive to overcome this is also verified.

Design Criteria Verification & Discussions

We now compare the design criteria obtained for our robot against the performance of the physical robot prototype. Upon testing the physical robot, it was found that the robot was able to climb a 120° slope with a minimum adhesive area of 7 cm^2 per flap. Fig. 14 shows image sequence of our robot climbing

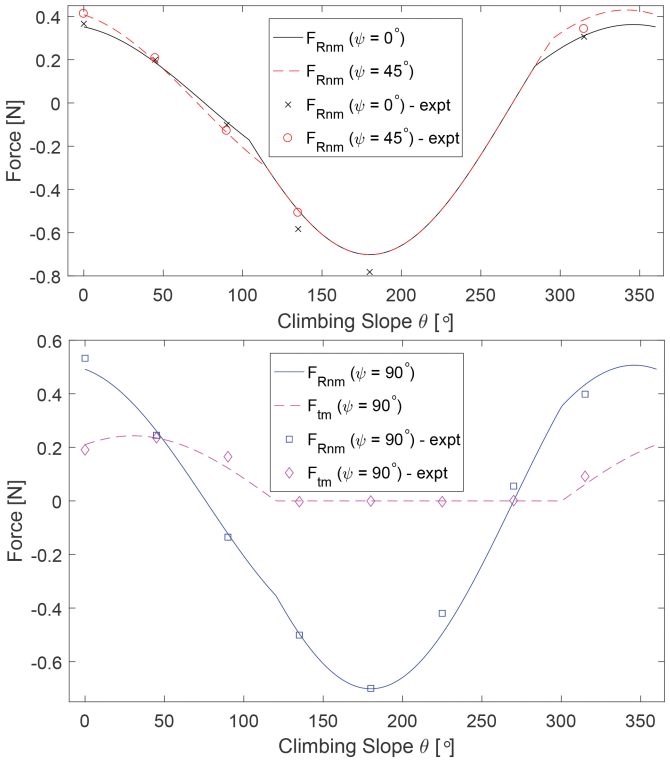

FIGURE 13. COMPARISON BETWEEN THEORETICAL AND EXPERIMENTAL VALUES OF THE NORMAL FORCE ON THE ADHESIVE AT THE BEGINNING ($\psi = 0°$) AND MIDDLE ($\psi = 45°$) OF SINGLE-FLAP STANCE (TOP), AND BOTH THE NORMAL FORCE ON THE ADHESIVE AND TAIL AT THE END ($\psi = 90°$) OF SINGLE-FLAP STANCE (BOTTOM).

a vertical surface during one of the tests. Although the design criteria underestimated the actual required adhesive area, it provides a reasonable guideline and starting estimate on the adhesive requirement. Possible reasons for the larger actual size required include incomplete contact area between the adhesive and the surface, non-ideal force transfer during the step, and overestima-

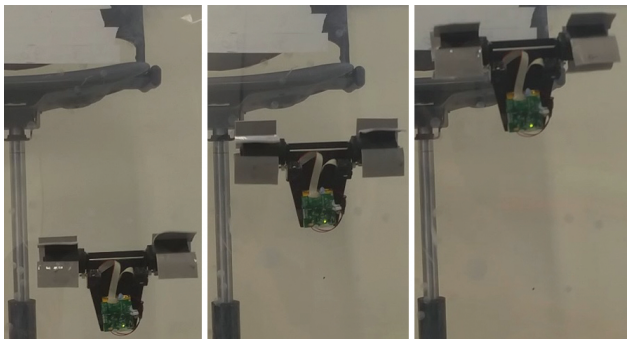

FIGURE 14. IMAGE SEQUENCE OF THE ROBOT CLIMBING A VERTICAL SURFACE.

tion of the adhesion performance curve as material test is usually conducted in a highly-controlled environment. It is also recommended [21] to have a margin of safety by increasing the area of the adhesive to circumvent those expected failures.

Based on Fig. 12, the torque required by each motor of our robot to climb slopes up to 120° is on average around 2 mNm. To verify the torque specification, we test the robot using two different motors: a low torque motor at 2.1 mNm (Faulhaber 1512U003SR 13:1 running at 75% continuous torque capacity) and a high torque motor at 14.85 mNm (Faulhaber 1512U003SR 112:1 running at 75% continuous torque capacity). The robot with the low torque motor was barely able to walk intermittently even on a 0° slope, while the robot with high torque motor climbed the slope up to 120° smoothly. These tests verify the motor torque criteria provided by the analysis.

The torque requirement analysis also provides explanation to the observation or experimental results in [17]. Their robot, which has a similar structure as our climbing robot, is capable of climbing on all slope angles. Hence, it will have a similar form of motor torque requirement plot as shown in Fig. 15, which is the plot of the required motor torque should our robot have been designed to climb on all slope angles ($F_{cr} = 0.71$ N from Fig. 8). Their robot was reported to climb slower vertically up than

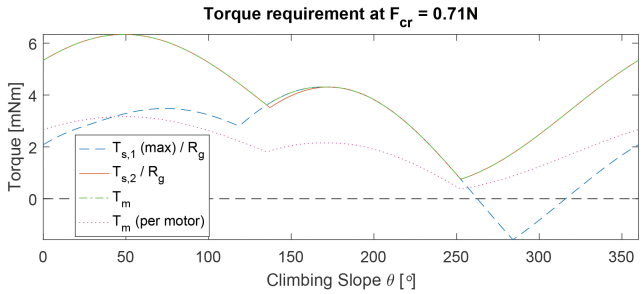

FIGURE 15. TORQUE REQUIREMENTS FOR CRITICAL PEELING FORCE DESIGNED TO CLIMB ALL SLOPE ANGLES.

inverted on the ceiling, which is verified by the higher motor torque required at 90° slope than at 180°. They also reported that the robot failed to walk vertically down due to the body rotating too much under its own weight during the single-flap stance. This is again verified by the motor torque requirement which shows a negative torque requirement for the single-flap stance at 270°, which is mainly attributed by the robot's weight component along the slope.

CONCLUSIONS

In this work, we expand on a previously-reported approach for climbing robot analysis and also apply it to the design of our climbing robot. Several refinements of the approach that were absent previously include integrating a robot motion model in order to obtain a more extensive and accurate force behavior analysis along the robot's motion, investigating the tail's effect on the climbing robot's overall equilibrium and requirements, as well as verification of the design criteria. Based on the more comprehensive analysis, we introduce and discuss two additional distinct states of the robot: when the robot's tail is in contact with the surface and when the robot's tail loses contact with the surface, which affects the overall force analysis of the climbing robot. The force behavior along the robot's motion as well as the two states of the robot's tail proposed in this paper are verified through experimental force measurements. Our future work will include sensitivity analysis on the developed model to optimally test and design the wheg configuration, as well as optimization of the drive train components and mass distribution.

ACKNOWLEDGMENT

The authors gratefully acknowledge the support of TL@SUTD-Systems Technology for Autonomous Reconnaissance & Surveillance and SUTD-MIT International Design Center (http://idc.sutd.edu.sg).

REFERENCES

[1] Chamanbaz, M., Mateo, D., Zoss, B. M., Tokić, G., Wilhelm, E., Bouffanais, R., & Yue, D. K. (2017). Swarm-enabling technology for multi-robot systems. *Frontiers in Robotics and AI, 4*, 12.

[2] B. Grocholsky, J. Keller, V. Kumar & G. Pappas (2006). Cooperative air and ground surveillance. *IEEE Robotics & Automation Magazine, 13*(3), 16-25.

[3] Satria, S., Foong, S., Soh, G. S., & Wood, K. L. (2017). Robust Variable Phase Shaper for vibration suppression of start-stop motion of a spherical rolling robot. *IEEE International Conference on Advanced Intelligent Mechatronics (AIM)* (pp. 1675-1681).

[4] Tan, N., Mohan, R. E., & Elangovan, K. (2016). Scorpio: A biomimetic reconfigurable rolling-crawling robot. *International Journal of Advanced Robotic Systems, 13*(5), 1729881416658180.

[5] Rybski, P. E., et al. (2000). Enlisting rangers and scouts for reconnaissance and surveillance. *IEEE Robotics & Automation Magazine, 7*(4), 14-24.

[6] Dan, Z., Tianmiao, W., Jianhong, L., & Guang, H. (2004). Modularization of miniature tracked reconnaissance robot. *IEEE International Conference on Robotics and Biomimetics (ROBIO)* (pp. 490-494).

[7] Xiao, J., Morris, W., Chakravarthy, N., & Calle, A. (2006). City climber: a new generation of mobile robot with wall-climbing capability. *Unmanned Systems Technology VIII* (pp. 62301D).

[8] Tâche, F., Fischer, W., Siegwart, R., Moser, R., & Mondada, F. (2007). Compact magnetic wheeled robot with high mobility for inspecting complex shaped pipe structures. *IEEE/RSJ International Conference on Intelligent Robots and Systems (IROS)* (pp. 261-266).

[9] Sintov, A., Avramovich, T., & Shapiro, A. (2011). Design and motion planning of an autonomous climbing robot with claws. *Robotics and Autonomous Systems, 59*(11), 1008-1019.

[10] Prahlad, H., Pelrine, R., Stanford, S., Marlow, J., & Kornbluh, R. (2008). Electroadhesive robotswall climbing robots enabled by a novel, robust, and electrically controllable adhesion technology. *IEEE International Conference on Robotics and Automation (ICRA)* (pp. 3028-3033).

[11] Daltorio, K. A., Gorb, S., Peressadko, A., Horchler, A. D., Ritzmann, R. E., & Quinn, R. D. (2006). A robot that climbs walls using micro-structured polymer feet. *International Conference on Climbing and Walking Robots (CLAWAR)* (pp. 131-138).

[12] Kim, S., Spenko, M., Trujillo, S., Heyneman, B., Santos, D., & Cutkosky, M. R. (2008). Smooth vertical surface climbing with directional adhesion. *IEEE Transactions on Robotics, 24*(1), 65-74.

[13] Unver, O., & Sitti, M. (2009). A miniature ceiling walking robot with flat tacky elastomeric footpads. *IEEE International Conference on Robotics and Automation (ICRA)* (pp. 2276-2281).

[14] Powelson, M. W., & Canfield, S. L. (2017). Design of Track-Based Climbing Robots Using Dry Adhesives. *ASME International Design Engineering Technical Conferences and Computers and Information in Engineering Conference (IDETC/CIE)* (pp. V05BT08A020).

[15] Raut, H. K., Baji, A., Hariri, H. H., Parveen, H., Soh, G. S., Low, H. Y., & Wood, K. L. (2018). Gecko-inspired Dry Adhesive Based on Micro-Nanoscale Hierarchical Arrays for Application in Climbing Devices. *ACS Applied Materials & Interfaces, 10*(1), 1288-1296.

[16] Sahay, R., Low, H. Y., Baji, A., Foong, S., & Wood, K. L. (2015). A State-of-the-Art Review and Analysis on the Design of Dry Adhesion Materials for Applications such as Climbing Micro-robots. *RSC Advances, 5*(63), 50821-50832.

[17] Breckwoldt, W. A., Daltorio, K. A., Heepe, L., Horchler, A. D., Gorb, S. N., & Quinn, R. D. (2015). Walking inverted on ceilings with wheel-legs and micro-structured adhesives. *IEEE/RSJ International Conference on Intelligent Robots and Systems (IROS)* (pp. 3308-3313).

[18] Murphy, M. P., Tso, W., Tanzini, M., & Sitti, M. (2006). Waalbot: An agile small-scale wall climbing robot utilizing pressure sensitive adhesives. *IEEE/RSJ International Conference on Intelligent Robots and Systems (IROS)* (pp. 3411-3416).

[19] Daltorio, K. A., Horchler, A. D., Gorb, S., Ritzmann, R. E., & Quinn, R. D. (2005). A small wall-walking robot with compliant, adhesive feet. *IEEE/RSJ International Conference on Intelligent Robots and Systems (IROS)* (pp. 3648-3653).

[20] Daltorio, K. A., Wei, T. E., Gorb, S. N., Ritzmann, R. E., & Quinn, R. D. (2007). Passive foot design and contact area analysis for climbing mini-whegs. *IEEE International Conference on Robotics and Automation (ICRA)* (pp. 1274-1279).

[21] Murphy, M. P., & Sitti, M. (2007). Waalbot: An agile small-scale wall-climbing robot utilizing dry elastomer adhesives. *IEEE/ASME Transactions on Mechatronics, 12*(3), 330-338.

[22] Carelli, C., Déplace, F., Boissonnet, L., & Creton, C. (2007). Effect of a gradient in viscoelastic properties on the debonding mechanisms of soft adhesives. *The Journal of Adhesion, 83*(5), 491-505.

[23] King, D. R., Bartlett, M. D., Gilman, C. A., Irschick, D. J., & Crosby, A. J. (2014). Creating GeckoLike Adhesives for "Real World" Surfaces. *Advanced Materials, 26*(25), 4345-4351.

[24] Bartlett, M. D., Croll, A. B., King, D. R., Paret, B. M., Irschick, D. J., & Crosby, A. J. (2012). Looking beyond fibrillar features to scale geckolike adhesion. *Advanced Materials, 24*(8), 1078-1083.

[25] Bartlett, M. D., Croll, A. B., & Crosby, A. J. (2012). Designing BioInspired Adhesives for Shear Loading: From Simple Structures to Complex Patterns. *Advanced Functional Materials, 22*(23), 4985-4992.

[26] Bartlett, M. D., & Crosby, A. J. (2014). High capacity, easy release adhesives from renewable materials. *Advanced Materials, 26*(21), 3405-3409.

[27] http://multimedia.3m.com/mws/media/1204168O/3m-vhb-tape-design-guide-high-res-pdf.pdf

[28] Liew, K. C. W. (2017). *Fabrication and characterization of biomimetic dry adhesives supported by foam backing material* (Master's thesis, University of Waterloo).

[29] Shahsavan, H., & Zhao, B. (2013). Bioinspired functionally graded adhesive materials: synergetic interplay of top viscouselastic layers with base micropillars. *Macromolecules, 47*(1), 353-364.

[30] McCarthy, J. M., & Soh, G. S. (2010). *Geometric Design of Linkages* (2^{nd} Ed.). Interdisciplinary Applied Mathematics. Springer Science & Business Media.

[31] He, Q., Yu, M., Li, Y., Chen, X., Zhang, H., Gong, L., & Dai, Z. (2014). Adhesion characteristics of a novel synthetic polydimethylsiloxane for bionic adhesive pads. *Journal of Bionic Engineering, 11*(3), 371-377.